Annealing-induced evolution of boron-doped polycrystalline diamond

Gufei Zhang [1,2,3,*] Ramiz Zulkharnay [4] Fabian Ganss,[5] Yujie Guo,[6] Mohammed Alkhalifah,[4] Limin Yang [4]
Sen Zhang,[1,2] Shengqiang Zhou [5] Peng Li,[7] Yejun Li [8] Victor V. Moshchalkov,[9] Jiaqi Zhu,[1,2] and Paul W. May [4,†]

[1]*National Key Laboratory of Science and Technology on Advanced Composites in Special Environments, Harbin Institute of Technology, 150080 Harbin, China*

[2]*Zhengzhou Research Institute, Harbin Institute of Technology, 450000 Zhengzhou, China*

[3]*POLIMA—Center for Polariton-Driven Light-Matter Interactions and Danish Institute for Advanced Study, University of Southern Denmark, Campusvej 55, DK-5230 Odense M, Denmark*

[4]*School of Chemistry, University of Bristol, Bristol BS8 1TS, United Kingdom*

[5]*Institute of Ion Beam Physics and Materials Research, Helmholtz-Zentrum Dresden-Rossendorf, Bautzner Landstraße 400, 01328 Dresden, Germany*

[6]*Photonics Research Group, Department of Information Technology, Ghent University-IMEC, 9052 Ghent, Belgium*

[7]*Department of Chemical Engineering, Shandong University of Technology, 255000 Zibo, China*

[8]*Hunan Key Laboratory of Nanophotonics and Devices, School of Physics and Electronics and School of Materials Science and Engineering, Central South University, 410083 Changsha, China*

[9]*Department of Physics and Astronomy, KU Leuven, B-3001 Heverlee, Belgium*

Diamond shows great promise for opening up new paradigms in the semiconductor industry and quantum electronics. Here, we investigate the influence of thermal annealing on the structural and electrical transport properties of heavily boron-doped polycrystalline diamond (BPD) thin films. Our structural analyses show that annealing beyond 600 °C can induce severe local amorphization in a BPD thin film and transform it into a binary mixture of spatially separate domains of amorphous carbon (a-C) and diamond grains. Due to this annealing-induced morphology and phase segregation, the BPD thin films demonstrate a significant decrease of the electron localization radius and a distinct increase of the Ginzburg-Landau coherence length. Our research provides physical insight into the conversion of diamond to a-C and aids in defining the application scope of BPD by revealing its heat tolerance.

I. INTRODUCTION

Nowadays, with the well-developed technique of chemical vapor deposition (CVD), cost-effective diamond can be deposited onto various substrate materials in different forms [1], making it possible to utilize its outstanding mechanical, optical, and electrical properties in a large variety of applications. For example, microelectronic processing techniques have been used to fabricate on-chip diamond nano- and micro-electromechanical systems that can enable high-precision sensing with low energy dissipation [2]. The photoregulation of Schottky barrier diodes based on oxygen-terminated diamond has been investigated to promote the efficiency of ultraviolet photon detection [3,4]. A two-dimensional hole gas at the interface of diamond and various oxides has been engineered through the method of surface transfer doping to advance field-effect transistors [5–8].

In contrast to surface charge transfer, boron doping allows for efficient tuning of the electrical properties of diamond over a wider range of conductivity. Upon low-concentration boron doping, diamond becomes semiconducting, due to the formation of an impurity band 0.37 eV above the valence band maximum. A further increase of the boron concentration leads to the broadening and shift of the impurity band towards the valence band, and an insulator-to-metal transition takes place in diamond at the critical doping threshold of about 3×10^{20} cm^{-3} [9,10]. Metallic diamond can be used for a variety of applications, in particular as electrochemical electrodes [11].

Along with the insulator-to-metal transition, heavily boron-doped diamond exhibits superconductivity at low temperatures [12–14]. Superconducting diamonds with polycrystalline morphology have been found to be extraordinarily rich in exotic quantum phenomena, e.g., an anomalous resistance peak prior to the superconducting transition [15], strong spatial modulation of the superconducting order parameter [16,17], and a superconducting anisotropy opposite to that of any other superconducting thin films [18]. These phenomena, arising from quantum confinement, suggest that superconducting nanodiamond grains separated by nonsuperconducting columnar grain boundaries could be exploited as nanoscale junctions to engineer superconducting quantum devices. Moreover, a recent investigation has demonstrated that the formation and trapping of Cooper pairs in nanoscale rings

made from heavily boron-doped diamond can give rise to an unconventional giant "magnetoresistance" [19], and such diamond nanorings may serve as artificial "atoms" for the physical implementation of charge qubits.

Given the fact that natural diamonds mined today were mostly brought to the Earth's surface by volcanic eruptions, one would naturally expect a high heat tolerance from their synthetic counterparts. This expectation seems to have been upheld by a study on boron-doped monocrystalline diamond where the superconductivity was first suppressed by helium ion implantation and then recovered to a certain extent through annealing at 1150 °C [20]. The question remains whether the more cost-effective polycrystalline diamond has the same degree of heat tolerance. Here, we address this question by investigating the evolution of the structural and electrical properties of heavily boron-doped polycrystalline diamond (BPD) thin films following different annealing temperatures. Our x-ray diffraction and Raman spectroscopy analyses combined with electrical transport measurements reveal that BPD films are rather vulnerable to heat, and annealing beyond 600 °C can cause substantial damage to the structure and electronic performance of the material. This may have serious implications for the use of BPD in high-temperature electronic applications.

II. EXPERIMENT

A. Diamond growth and annealing

Heavily BPD films were deposited on an undoped (100) Si substrate (with a 300-nm-thick capping layer of SiO_2) using hot-filament-assisted CVD as described in our previous work [17–19]. Nanodiamond suspension was employed to seed the Si substrates before CVD growth via an electrostatic seeding technique [21]. A flow of a gas mixture comprising 1% CH_4 in H_2 was used for the CVD process, while boron doping was achieved by addition to the gas feedstock of B_2H_6 at a B:C ratio of 8750 ppm. Feedstock gases with a total gas flow of 202.6 standard cubic centimeters per minute at STP were controlled using independent mass flow controllers, while the chamber pressure was set to 20 torr. An 850-nm-thick BPD continuous layer with a boron concentration of $\sim 4 \times 10^{21}$ cm^{-3} (previously determined using secondary ion mass spectrometry) on SiO_2/Si was achieved within 75 min. The charge-carrier density of the as-grown BPD films was determined to be about 3.3×10^{21} cm^{-3} through Hall effect measurements by neglecting the influence of the granular disorder on the electrical transport. The difference between the boron concentration and the charge-carrier density suggests that the boron dopants are not all substitutionally incorporated into the diamond lattice, and approximately 18% of them are introduced into the material as deep-level impurities and/or trapped in the grain boundaries [22].

A horizontal quartz tube furnace (EHA 12/300B, Carbolite Gero Ltd.) was employed for the high-temperature annealing of the BPD samples. The samples were annealed in flowing Ar (325 ml min^{-1}) at atmospheric pressure from room temperature up to 800 °C at a ramp rate of 5 °C min^{-1}, held at this temperature for 20 min, and then allowed to cool to room temperature under an Ar atmosphere.

B. Structural analyses using x-ray diffraction and Raman spectroscopy

Grazing-incidence x-ray diffraction (GIXRD) measurements were performed for qualitative phase analysis, using a parallel-slit analyzer to yield a better signal-to-noise ratio than in the symmetrical geometry and to suppress substrate reflections. The parallel beam of Cu $K\alpha$ radiation was incident at a constant angle of 0.5°. The phase analysis was done with Rigaku's SMARTLAB STUDIO II software and ICDD's PDF-4+ database [23].

Laser Raman spectroscopy using a confocal micro-Raman system (Renishaw RM 2000 using WIRE 2.0 software) was carried out to investigate the impact of annealing-temperature variations on the BPD lattice distortion. An Ar$^+$ laser with a wavelength of 514 nm (visible green light) was used as an excitation source. The laser exposure, accumulation time, and laser power were set to 10 s, 5 s, and 33%, respectively, in order to optimize the signal-to-noise ratio in the resulting patterns.

C. Electrical transport measurements

The electrical transport properties of the samples were characterized through four-probe ac measurements in a ^{4}He cryostat. The cryostat was equipped with a dc magnet allowing electrical transport measurements in the temperature range of 1.5–300 K at different applied magnetic fields. A low-frequency current of 5 µA was sent through the samples for excitation, and a lock-in amplifier was used to measure the resistance.

III. RESULTS AND DISCUSSION

Figure 1(a) shows the GIXRD patterns of our samples. The polycrystalline nature of the thin films is revealed by the presence of multiple diffraction peaks, (111), (220), and (311), from diamond. By using Bragg's law, we calculated the diamond lattice parameter from the (111) peak. As shown in Fig. 1(c), the annealing temperature, T_{ann}, barely exerts an influence on the diamond lattice parameter. However, as T_{ann} is increased beyond 600 °C, the characteristic diffraction peaks of diamond become diminished in intensity, indicating the amorphization of the structure. This is further confirmed by an abrupt increase of the full width at half maximum (FWHM) of the (111) peak above 600 °C [Fig. 1(d)]. Another intriguing feature of the T_{ann} dependence of the FWHM lies in its slight decline below 600 °C, which suggests that the influence of annealing on the BPD thin films might be twofold, i.e., low-temperature annealing can aid in restoring the crystalline structure of heavily boron-doped diamond grains to an extent, whereas high-temperature annealing enhances the degree of disorder of the system. Figure 1(e) shows the T_{ann} dependence of the integrated intensity of the diamond (111) peak, which suggests that annealing above 600 °C leads to a significant reduction in the volume of diamond.

Besides the characteristic diamond peaks, diffraction peaks from silicon carbide are also found in the GIXRD patterns [Fig. 1(a)], which probably originate from the interface between the BPD and the Si substrate. Further additional peaks
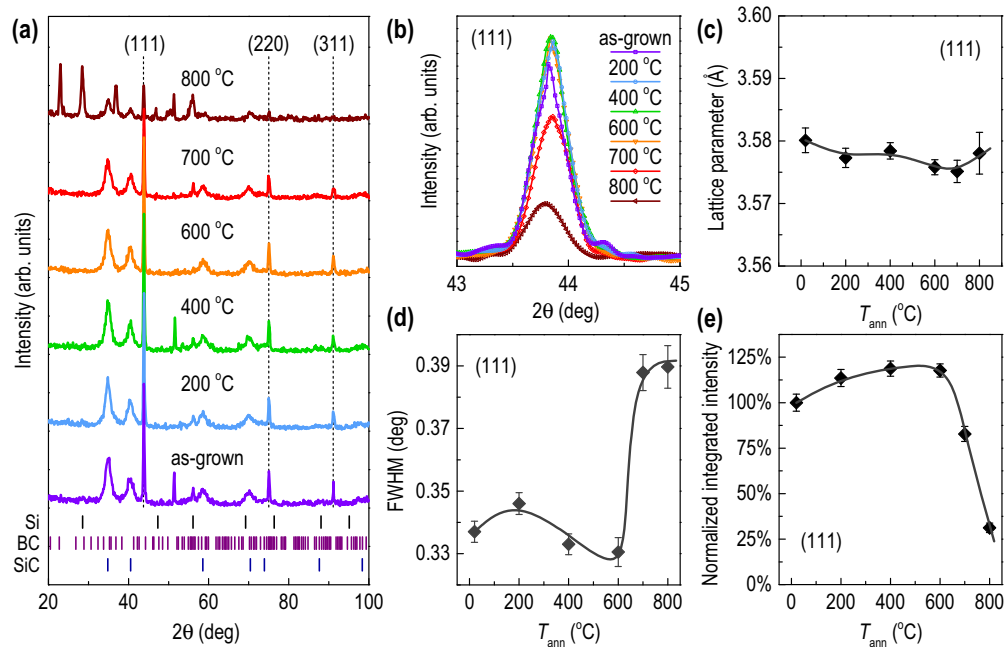
FIG. 1. Annealing-induced structural evolution of BPD as measured by GIXRD. (a) GIXRD patterns of the as-grown and annealed BPD thin films. The diffraction peaks from polycrystalline diamond, i.e., (111), (220), and (311), are labeled with dashed lines. The short bars denote signals from the substrate, boron carbide, and silicon carbide, respectively. The origin of the peak at 51.4 ° remains unknown. (b) Magnification of the (111) diffraction peak from diamond. (c) The diamond lattice parameter calculated from the (111) peak. The data point of the as-grown BPD thin film is set at 20 °C in the plot. (d) FWHM of the (111) peak as a function of the annealing temperature. (e) The normalized integrated intensity of the (111) peak as a function of the annealing temperature. The curves in panels (c)–(e) serve as visual guides.

observed in the sample annealed at $T_{ann} = 800$ °C are indicative of the formation of boron carbide.

To investigate the influence of T_{ann} on the amorphization of BPD, Raman-scattering measurements were performed. Figure 2(a) presents the Raman spectra measured over various ranges of annealing temperature, from the pristine BPD (labeled "as-grown") to 800 °C. The band around 500 cm^{-1} originates from local vibrational modes of boron pairs [24], which cause some distortion in the diamond lattice around these isolated defects [25]. The prominent bands in the range of 1000 and 1300 cm^{-1} have been deconvoluted into four peaks (indicated as Peaks 1, 2, 3, and 4) [Fig. 2(b)], while the a-C region at ~ 1520 cm^{-1} is labeled with an arrow [Fig 2(a)] [26,27]. In particular, the minimum phonon density observed in diamond, arising at ~ 1000 cm^{-1}, is assigned to Peak 1 [19]. The zone-center phonon line of diamond at 1332 cm^{-1} (Peak 4) is typically distorted for BPD due to the high boron concentration (known as the Fano effect) [28]. Therefore, this results in a shift to a lower wave number of 1293 cm^{-1} from its original position, in good agreement with previous studies [19,29,30]. It is important to note that Peaks 2 and 3, attributed to the symmetry disorder resulting from high boron doping, are relevant [31,32]. However, Peak 3, with its higher concentration compared to Peak 2, is our primary focus in this study. As shown in Figs. 2(c)–2(e), all three characteristic peaks for BPD exhibited a shift to a lower wave number with increased T_{ann}, indicating that amorphization is induced in the material upon annealing. Specifically, the most prominent shift was detected at $T_{ann} = 600$ °C, marking the exacerbation of the amorphization. As a result, with a further increase of T_{ann} (e.g., 800 °C), the characteristic peak of a-C exhibits a broad feature

compared to that of lower annealing temperatures, suggesting a higher amorphization nature of the surface and aligning well with the GIXRD data.

Figure 3 shows the morphological evolution of BPD upon annealing. As illustrated by the scanning electron microscopy (SEM) images, the BPD thin film already starts demonstrating minute traces of local amorphization at a relatively low T_{ann} of 200 °C [Fig. 3(b)]. A further increase of T_{ann} leads to the proliferation of amorphous spots where the sharp edges between the facets of diamond grains gradually smear out [Fig. 3(c)]. When increasing T_{ann} beyond 600 °C, the amorphous spots coalesce into a-C domains, in stark contrast to the remaining BPD [Figs. 3(d) and 3(f)]. At $T_{ann} = 800$ °C, the severely amorphized areas evolve into a cracked structure where the mixture of sp^2 and sp^3 carbon-bonding types are separated by fissures [Fig. 3(e)].

Apart from altering the structure of BPD, annealing also brings changes to its electrical transport properties. Figure 4(a) shows the temperature dependence of the resistivity, $\rho(T)$, of the BPD samples. The normal-state resistivity of the system is significantly increased upon annealing, in particular when $T_{ann} \geqslant 600$ °C.

To provide a different perspective on the annealing-induced evolution of the electrical transport in the system, the $\rho(T)$ curves were normalized to their respective resistivity values at 300 K for ease of comparison [Fig. 4(b)]. The as-grown BPD thin film shows a crossover from a positive to a negative temperature coefficient of resistivity at about 210 K. Such a crossover has been observed in many doped insulators, such as high-temperature superconductors [33,34], which exhibit a metal-like behavior with $d\rho/dT > 0$ at high temperatures,
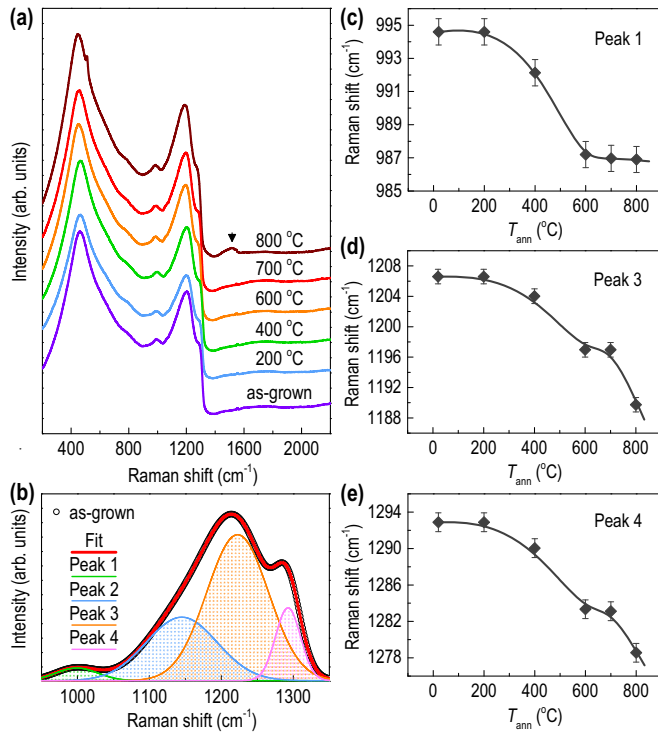
FIG. 2. Laser Raman spectra acquired for surface structural characterization of the BPD films. (a) A set of spectra for the as-grown and annealed BPD films. The spectra have been vertically offset for clarity. Black arrow: the characteristic peak of a-C with a broad feature. (b) Deconvoluted example peak from the as-grown sample, with photoluminescent background subtraction to give a flat baseline. In panels (c), (d), and (e), Raman shifts are depicted as a function of annealing temperature for Peaks 1, 3, and 4, respectively. The curves serve as visual guides.

FIG. 4. Annealing-induced evolution of the electrical transport properties of BPD. (a) Thermoresistivity (resistivity, ρ, as a function of temperature, T) of the as-grown and annealed BPD thin films. (b) Thermoresistivity curves normalized to their respective values at 300 K. (c) Resistive superconducting transitions in the samples. (d) Annealing-induced changes of the superconducting transition temperature acquired by setting the criterion as 98% of the resistivity at 8 K. The curve is a guide to the eye.
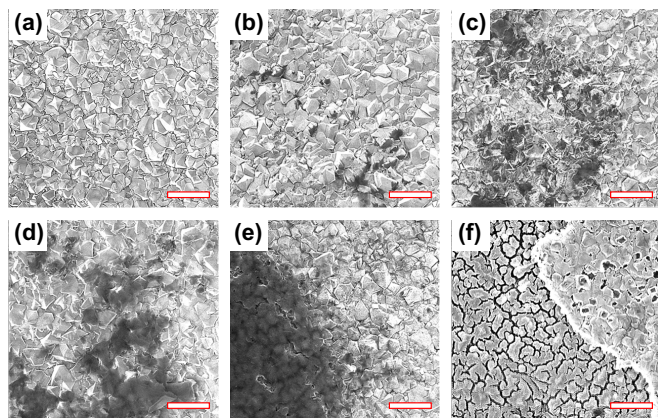

FIG. 3. Annealing-induced morphological evolution of BPD as revealed by SEM imaging. (a) In the as-grown BPD thin film, the diamond grains show sharp facetted edges. (b) At the surface of the BPD thin film annealed at 200 °C, traces of local amorphization are found as minute dark spots. As T_{ann} is increased up to (c) 400 °C, (d) 600 °C, and (e) 700 °C, the proliferation of amorphous spots leads to the disappearance of diamond facets in certain areas and the formation of a-C domains. (f) At $T_{\text{ann}} = 800$ °C, the severely amorphized areas evolve into a fissured structure, and pinholes are introduced in the less amorphized areas where blunted diamond facets are still present. The white scale is 2 μm in all cases.
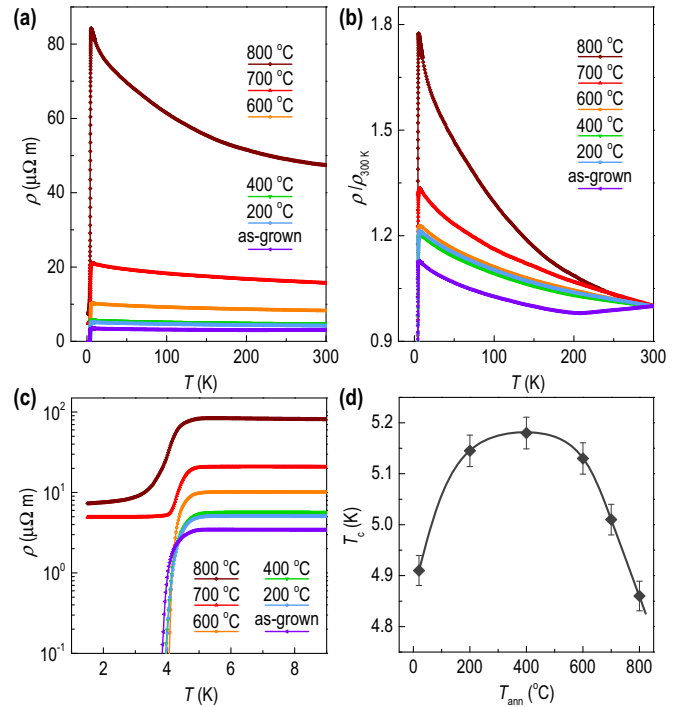
and reveal their semiconductor or doped-insulator nature with $d\rho/dT < 0$ at low temperatures. In contrast, the annealed BPD thin films all show a monotonic $\rho(T)$ dependence with $d\rho/dT < 0$ prior to their resistive superconducting transition. Furthermore, when increasing T_{ann}, the absolute value of $d\rho/dT$ is substantially enhanced, in particular at low temperatures. These features clearly indicate that upon annealing, the normal state of the system is driven towards an insulating state rather than a metallic state [22].

The superconductivity in the BPD thin films turns out to be rather robust. As T_{ann} is increased beyond 600 °C, despite the severe amorphization and phase segregation induced by annealing, the system still exhibits a resistive superconducting transition. Nevertheless, in this case, no zero-resistance state is observed in the electrical transport measurements [Fig. 4(c)].

A BPD thin film can be treated as a resistor network as shown in Fig. 5, given that the metallic diamond grains are separated by highly resistive columnar grain boundaries [22,35]. At low temperatures, the resistor network transforms into a network of grain-boundary-grain Josephson junctions [22,35,36]. In this Josephson junction network, the intergrain phase coherence will give rise to a resistive superconducting transition, and the establishment of percolation pathways for Cooper pairs across the network will enable the emergence of a superconducting state with zero resistance [Fig. 5(a)].
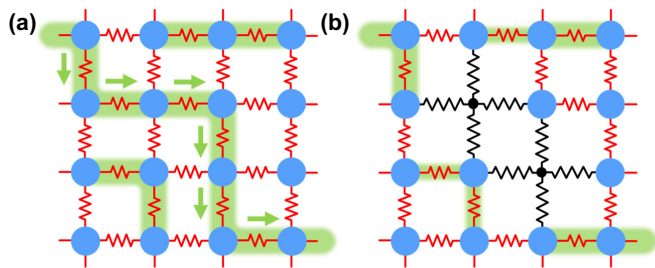
FIG. 5. Representation of BPD thin films as a resistor network. The heavily boron-doped diamond grains (blue) are metallic at high temperatures and superconducting at low temperatures. In either case, the diamond grains are interconnected by highly resistive columnar grain boundaries, which can be treated as resistors (red). (a) In an as-grown BPD thin film, due to intergrain coupling (green strokes), a percolation path (green arrows) is established for Cooper pairs, giving rise to the emergence of a superconducting state. (b) Upon high-temperature annealing, severe local amorphization (resistors in black) and phase segregation are induced in BPD thin films, leading to the truncation of the percolation path and thus the absence of the superconducting state.

Upon high-temperature annealing, severe morphological and phase segregation can result in the truncation of the percolation pathways, which will, in turn, lead to the absence of the superconducting state [Fig. 5(b)]. Due to the local phase coherence preserved within the remaining domains of superconducting nanodiamond grains, the BPD films annealed at high temperatures still show a resistive superconducting transition [Figs. 4(c) and 5(b)].

By setting the criteria at 98% of the resistivity at 8 K for an approximation of the onset of the resistive superconducting transition, we obtain the T_c-T_{ann} dependence shown in Fig. 4(d). At low T_{ann}, the T_c increases, which may be due to the annealing-driven incorporation of interstitial boron dopants into the diamond crystal lattice. Note that in the case of BPD, a higher boron concentration in the diamond grains does not necessarily give rise to a decrease in the normal-state resistivity and $d\rho/dT$, because the normal-state transport properties of such materials are dominated by the high-resistance grain boundaries filled with a-C and boron rather than the diamond grains (Fig. 5) [22,35,36].

A further increase of T_{ann} leads to the decrease of T_c, suggesting that a thermal treatment beyond 400 °C already starts generating structural imperfections that suppress the intergrain coupling and/or intragrain superconductivity. The suppression of superconductivity is exacerbated, as T_{ann} increases beyond 600 °C. Note that the diamond grains are not free of disorder, due to the presence of a high concentration of boron dopants (impurities), doping-induced defects, and twin boundaries [16,18]. As reflected by the blunted diamond facets and the pinholes in the BPD films annealed at high temperatures [Figs. 3(c)–3(e)], the intragrain disorder may also play a role in instigating local amorphization, which will, in turn, supress the intragrain superconductivity.

To gain further insight into the influence of annealing on the superconductivity in BPD, the magnetic-field-driven superconducting-normal transition in the samples was measured, enabling their Ginzburg-Landau coherence length, ξ_{GL},
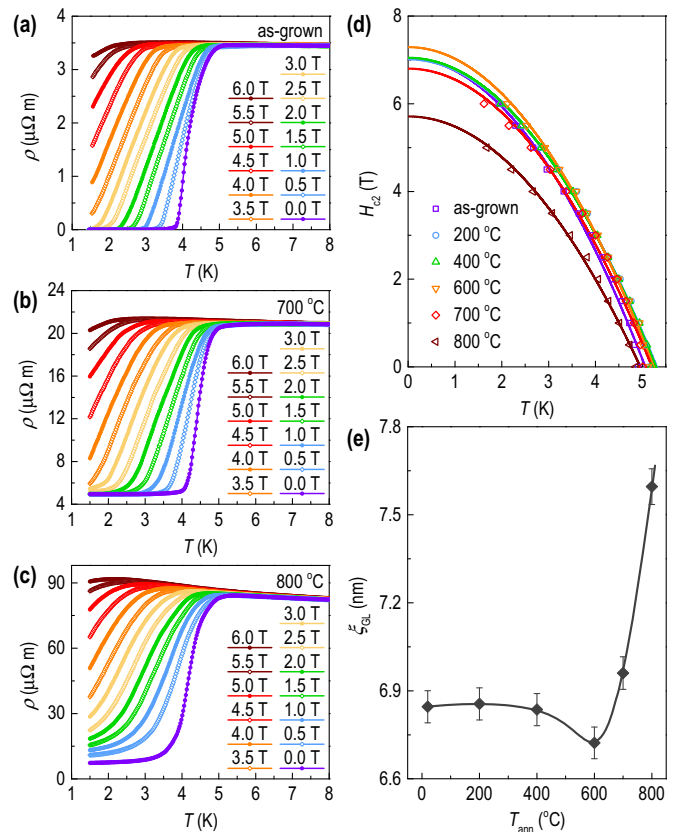

FIG. 6. (a) Magnetic-field dependence of the resistive superconducting transition in the as-grown BPD thin film and the samples annealed at (b) 700 °C and (c) 800 °C, respectively. The data for the samples annealed at other temperatures (i.e., 200 °C, 400 °C, and 600 °C) closely resemble those of the as-grown BPD, and thus are not shown. (d) Phase boundaries of the as-grown BPD and annealed samples. The temperature dependences of the upper critical magnetic fields are extrapolated down to zero temperature through quadratic fits (curves). (e) The Ginzburg-Landau coherence length as a function of the annealing temperature. The curve is a guide to the eye.

to be deduced (Fig. 6). The data from the samples annealed at 200–600 °C show a close resemblance to those of the as-grown BPD thin film, and thus are not shown. By using the same criterion as for the determination of T_c, the temperature dependences of the upper critical magnetic fields, H_{c2}, were obtained, enabling the H_{c2}-T phase diagram to be constructed, as shown in Fig. 6(d).

The quadratic fits of the H_{c2}-T phase boundaries are extrapolated down to zero temperature for the acquisition of $H_{c2}(0\,K)$, which enables the derivation of $\xi_{GL} = [\Phi_0/2\pi H_{c2}(0\,K)]^{0.5}$ with Φ_0 being the magnetic flux quantum [37]. Taking the coherence length of a monocrystalline diamond, $\xi_0 = 15$ nm [14], the mean free path, l, can be derived from $\xi_{GL} \sim (l\xi_0)^{0.5}$. The mean free path is estimated to be 3.1 nm in the as-grown BPD thin film and the samples annealed at 200–400 °C, 3.0 nm in the sample annealed at 600 °C, 3.2 nm in the sample annealed at 700 °C, and 3.8 nm in the sample annealed at 800 °C. The resulting ξ_{GL}/l ratio is ~ 2 for all samples, indicating that the as-grown and annealed BPD films are rather "dirty" superconductors.
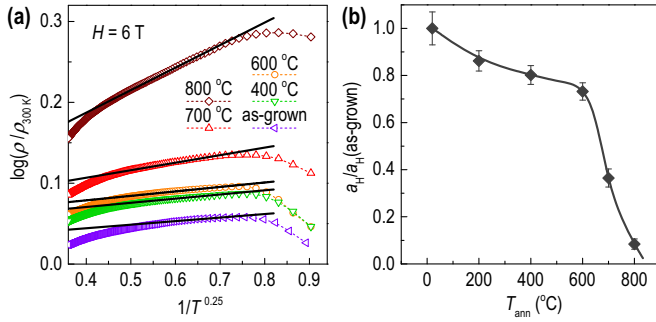
FIG. 7. Analysis of the conduction mechanism in the BDP thin films. (a) A magnetic field of 6 T was applied to suppress the superconductivity at low temperatures, such that the normal state of the samples can be restored over a wider temperature range for analyzing the fermion hopping mechanism. Black lines: linear fits with respect to Mott's law in three dimensions. Due to the remnant superconductivity below 2.9 K, the normalized $\rho(T)$ curves deviate from their linear fits. (b) Annealing-induced changes of the localization radius, which is normalized to the value of the as-grown BPD thin film.

Consistent with the significant changes in the T_{ann} dependence of the FWHM of the diamond (111) peak and the T_{ann} dependence of the Raman shifts [Figs. 1(d) and 2(c)–2(e)], the ξ_{GL}-T_{ann} dependence also demonstrates a slight decrease below 600 °C followed by an upturn at higher T_{ann} [Fig. 6(e)]. The overall consistency between these data indicates that the superconductivity in BPD is highly correlated with the degree of disorder of the diamond grains, and the origin of the superconductivity cannot be attributed to the boron-enriched amorphous carbon in the grain boundaries as argued by some previous studies [38].

As shown in Fig. 5, a BPD thin film can be treated as a resistor network that bears a great resemblance to Mott's site lattice model. In Ref. [22], by treating the heavily boron-doped diamond grains as giant dopants incorporated into the resistor network, we had justified the use of Mott's law in three dimensions (3D) for analyzing the conduction mechanism of BPD thin films. To enable the analysis of the conduction mechanism of single quasiparticles, the superconductivity in the samples needs to be suppressed by high magnetic fields. As shown in Fig. 7(a), at low temperatures, the $\rho(T)$ curves measured at 6 T are found to be in fairly good agreement with Mott's law in 3D, $\rho = \rho_0 \exp\{(T_0/T)^{0.25}\}$, where T_0 characterizes the strength of the single quasiparticle correlation [39,40]. Because the applied magnetic fields are not high enough to fully suppress the superconductivity below 2.9 K [Figs. 6(a)–6(c)], the $\rho(T)$ curves deviate from their linear fits.

Figure 7(b) shows the T_{ann} dependence of the localization radius at boron sites, $a_H \sim T_0^{-1/3}$ [22,40], derived from the linear fits in Fig. 7(a). As T_{ann} increases, a_H continues to decrease, indicating that the localization of single

quasiparticles in the BPD is enhanced upon annealing, which explains the increase of the normal-state resistivity. Above 600 °C, a_H demonstrates a sharp decrease, which coincides with the severe morphology and phase segregation revealed by our GIXRD, Raman spectroscopy, and SEM measurements (see Figs. 1–3) and suggests that high-temperature annealing can give rise to a metal-insulator transition in BPD.

IV. CONCLUSION

In summary, the heat tolerance of highly boron-doped polycrystalline diamond was studied by investigating the evolution of its structural and electronic properties as a function of annealing temperature. Our data indicate that low-temperature annealing can slightly heal the crystal lattice of heavily boron-doped diamond grains, thus slightly promoting the superconductivity of the system. However, once the annealing temperature is increased beyond a critical point at about 600 °C, severe morphology and phase segregation takes place, leading to an abrupt decline in the superconducting properties and normal-state conductivity of this material. Taking into account the behavior of annealed monocrystalline diamond [20], the grain and twin boundaries might be responsible for the fairly low heat tolerance of BPD by instigating the local amorphization and phase segregation during annealing. These results have important implications for the use of BPD in high-temperature electronic applications, as severe degradation of device performance may occur if the devices are operated above 600 °C. Even for operation at temperatures lower than this threshold, the slow degradation of the material properties may lead to shorter device lifetimes. Considering that high-temperature electronics is one area where diamond is suggested to outperform competing materials, further work on boron segregation at these temperatures is urgently needed.

[1] P. W. May, Diamond thin films: A 21st-century material, Philos. Trans. R. Soc., A **358**, 473 (2000).

[2] M. Liao, L. Sang, T. Teraji, S. Koizumi, and Y. Koide, Ultrahigh performance on-chip single crystal diamond NEMS/MEMS

with electrically tailored self-sensing enhancing actuation, Adv. Mater. Technol. **4**, 1800325 (2019).

[3] M. Liao, Y. Koide, and J. Alvarez, Single Schottky-barrier photodiode with interdigitated-finger geometry:

Application to diamond, Appl. Phys. Lett. **90**, 123507 (2007).

[4] X. Zhang, K. Liu, B. Liu, B. Dai, Y. Zhang, and J. Zhu, Phenomenon of photo-regulation on gold/diamond Schottky barriers and its detector applications, Appl. Phys. Lett. **122**, 062106 (2023).

[5] K. G. Crawford, L. Cao, D. Qi, A. Tallaire, E. Limiti, C. Verona, A. T. S. Wee, and D. A. J. Moran, Enhanced surface transfer doping of diamond by V_2O_5 with improved thermal stability, Appl. Phys. Lett. **108**, 042103 (2016).

[6] S. A. O. Russell, L. Cao, D. Qi, A. Tallaire, K. G. Crawford, A. T. S. Wee, and D. A. J. Moran, Surface transfer doping of diamond by MoO_3: A combined spectroscopic and Hall measurement study, Appl. Phys. Lett. **103**, 202112 (2013).

[7] A. Daicho, T. Saito, S. Kurihara, A. Hiraiwa, and H. Kawarada, High-reliability passivation of hydrogen-terminated diamond surface by atomic layer deposition of Al_2O_3, J. Appl. Phys. **115**, 223711 (2014).

[8] C. Verona, M. Benetti, D. Cannatà, W. Ciccognani, S. Colangeli, F. D. Pietrantonio, E. Limiti, M. Marinelli, and G. Verona-Rinati, Stability of H-terminated diamond MOSFETs with V_2O_5/Al_2O_3 as gate insulator, IEEE Electron Device Lett. **40**, 765 (2019).

[9] T. Klein, P. Achatz, J. Kacmarcik, C. Marcenat, F. Gustafsson, J. Marcus, E. Bustarret, J. Pernot, F. Omnes, Bo E. Sernelius, C. Persson, A. Ferreira da Silva, and C. Cytermann, Metal-insulator transition and superconductivity in boron-doped diamond, Phys. Rev. B **75**, 165313 (2007).

[10] G. Zhang, Superconductivity in diamond films and other nanogranular materials, Ph.D. thesis, KU Leuven, 2013.

[11] Y. Einaga, Boron-doped diamond electrodes: Fundamentals for electrochemical applications, Acc. Chem. Res. **55**, 3605 (2022).

[12] E. A. Ekimov, V. A. Sidorov, E. D. Bauer, N. N. Mel'nik, N. J. Curro, J. D. Thompson, and S. M. Stishov, Superconductivity in diamond, Nature (London) **428**, 542 (2004).

[13] Y. Takano, M. Nagao, I. Sakaguchi, M. Tachiki, T. Hatano, K. Kobayashi, H. Umezawa, and H. Kawarada, Superconductivity in diamond thin films well above liquid helium temperature, Appl. Phys. Lett. **85**, 2851 (2004).

[14] E. Bustarret, J. Kačmarčik, C. Marcenat, E. Gheeraert, C. Cytermann, J. Marcus, and T. Klein, Dependence of the superconducting transition temperature on the doping level in single-crystalline diamond films, Phys. Rev. Lett. **93**, 237005 (2004).

[15] G. Zhang, M. Zeleznik, J. Vanacken, P. W. May, and V. V. Moshchalkov, Metal–bosonic insulator–superconductor transition in boron-doped granular diamond, Phys. Rev. Lett. **110**, 077001 (2013).

[16] G. Zhang, S. Turner, E. A. Ekimov, J. Vanacken, M. Timmermans, T. Samuely, V. A. Sidorov, S. M. Stishov, Y. Lu, B. Deloof, B. Goderis, G. Van Tendeloo, J. Van de Vondel, and V. V. Moshchalkov, Global and local superconductivity in boron-doped granular diamond, Adv. Mater. **26**, 2034 (2014).

[17] G. Zhang, T. Samuely, J. Kačmarčík, E. A. Ekimov, J. Li, J. Vanacken, P. Szabó, J. Huang, P. J. Pereira, D. Cerbu, and V. V. Moshchalkov, Bosonic anomalies in boron-doped polycrystalline diamond, Phys. Rev. Appl. **6**, 064011 (2016).

[18] G. Zhang, J. Kačmarčík, Z. Wang, R. Zulkharnay, M. Marcin, X. Ke, S. Chiriaev, V. Adashkevich, P. Szabó, Y. Li, P. Samuely, V. V. Moshchalkov, P. W. May, and H.-G. Rubahn, Anomalous anisotropy in superconducting nanodiamond films induced by crystallite geometry, Phys. Rev. Appl. **12**, 064042 (2019).

[19] G. Zhang, R. Zulkharnay, X. Ke, M. Liao, L. Liu, Y. Guo, Y. Li, H.-G. Rubahn, V. V. Moshchalkov, and P. W. May, Unconventional giant "magnetoresistance" in bosonic semi-conducting diamond nanorings, Adv. Mater. **35**, 2211129 (2023).

[20] D. L. Creedon, Y. Jiang, K. Ganesan, A. Stacey, T. Kageura, H. Kawarada, J. C. McCallum, B. C. Johnson, S. Prawer, and D. N. Jamieson, Irradiation-induced modification of the superconducting properties of heavily-boron-doped diamond, Phys. Rev. Appl. **10**, 044016 (2018).

[21] O. J. L. Fox, J. O. P. Holloway, G. M. Fuge, P. W. May, and M. N. R. Ashfold, Electrospray deposition of diamond nanoparticle nucleation layers for subsequent CVD diamond growth, *Diamond Electronics and Bioelectronics—Fundamentals to Applications III*, MRS Online Proceedings Library 1203, J17 (2009).

[22] G. Zhang, S. Janssens, J. Vanacken, M. Timmermans, J. Vacík, G. W. Ataklti, W. Decelle, W. Gillijns, B. Goderis, K. Haenen, P. Wagner, and V. V. Moshchalkov, Role of grain size in superconducting boron-doped nanocrystalline diamond thin films grown by CVD, Phys. Rev. B **84**, 214517 (2011).

[23] ICDD, Silicon 00-026-1481; boron carbide 03-065-2860; silicon carbide 04-008-7773; powder diffraction file PDF-4+, 2022.

[24] M. Bernard, C. Baron, and A. Deneuville, About the origin of the low wave number structures of the Raman spectra of heavily boron doped diamond films, Diamond Relat. Mater. **13**, 896 (2004).

[25] J. P. Goss and P. R. Briddon, Theory of boron aggregates in diamond: First-principles calculations, Phys. Rev. B **73**, 085204 (2006).

[26] A. C. Ferrari and J. Robertson, Raman spectroscopy of amorphous, nanostructured, diamond–like carbon, and nanodiamond, Philos. Trans. R. Soc., A **362**, 2477 (2004).

[27] M. Yoshikawa, G. Katagiri, H. Ishida, and A. Ishitani, Raman spectra of diamondlike amorphous carbon films, Solid State Commun. **66**, 1177 (1988).

[28] Y. A. Sorb, F. P. Bundy, and R. C. DeVries, Diamond: High-pressure synthesis, *Reference Module in Materials Science and Materials Engineering* (Elsevier, Amsterdam, 2016).

[29] P. W. May, W. J. Ludlow, M. Hannaway, P. J. Heard, J. A. Smith, and K. N. Rosser, Raman and conductivity studies of boron doped microcrystalline diamond, facetted nanocrystalline diamond and cauliflower diamond films, Diamond Relat. Mater. **17**, 105 (2008).

[30] V. Mortet, Z. Vlčková Živcová, A. Taylor, O. Frank, P. Hubík, D. Trémouilles, F. Jomard, J. Barjon, and L. Kavan, Insight into boron-doped diamond Raman spectra characteristic features, Carbon **115**, 279 (2017).

[31] P. Knittel, R. Stach, T. Yoshikawa, L. Kirste, B. Mizaikoff, C. Kranz, and C. E. Nebel, Characterisation of thin boron-doped diamond films using Raman spectroscopy and chemometrics, Anal. Methods **11**, 582 (2019).

[32] V. Mortet, A. Taylor, Z. Vlčková Živcová, D. Machon, O. Frank, P. Hubík, D. Tremouilles, and L. Kavan, Analysis of heavily boron-doped diamond Raman spectrum, Diamond Relat. Mater. **88**, 163 (2018).

[33] H.-B. Jang, J. S. Lim, and C.-H. Yang, Film-thickness-driven superconductor to insulator transition in cuprate superconductors, Sci. Rep. **10**, 3236 (2020).

[34] G. S. Boebinger, Yoichi Ando, A. Passner, T. Kimura, M. Okuya, J. Shimoyama, K. Kishio, K. Tamasaku, N. Ichikawa, and S. Uchida, Insulator-to-metal crossover in the normal state of $La_{2−x}Sr_xCuO_4$ near optimum doping, Phys. Rev. Lett. **77**, 5417 (1996).

[35] G. Zhang, T. Samuely, H. Du, Z. Xu, L. Liu, O. Onufriienko, P. W. May, J. Vanacken, P. Szabó;, J. Kačmarčík, H. Yuan, P. Samuely, R. E. Dunin-Borkowski, J. Hofkens, and V. V. Moshchalkov, Bosonic confinement and coherence in disordered nanodiamond arrays, ACS Nano **11**, 11746 (2017).

[36] G. Zhang, Y. Zhou, S. Korneychuk, T. Samuely, L. Liu, P. W. May, Z. Xu, O. Onufriienko, X. Zhang, J. Verbeeck, P. Samuely, V. V. Moshchalkov, Z. Yang, and H.-G. Rubahn,

Superconductor-insulator transition driven by pressure-tuned intergrain coupling in nanodiamond films, Phys. Rev. Mater. **3**, 034801 (2019).

[37] K. Fossheim and A. Sudbø, *Superconductivity: Physics and Applications* (Wiley, London, 2004), pp. 182–183.

[38] N. Dubrovinskaia, R. Wirth, J. Wosnitza, T. Papageorgiou, H. F. Braun, N. Miyajima, and L. Dubrovinsky, An insight into what superconducts in polycrystalline boron-doped diamonds based on investigations of microstructure, Proc. Natl. Acad. Sci. USA **105**, 11619 (2008).

[39] N. F. Mott, Conduction in glasses containing transition metal ions, J. Non-Cryst. Solids **1**, 1 (1968).

[40] C. Quitmann, D. Andrich, C. Jarchow, M. Fleuster, B. Beschoten, G. Güntherodt, V. V. Moshchalkov, G. Mante, and R. Manzke, Scaling behavior at the insulator-metal transition in $Bi_2Sr_2(Ca_zR_{1−z})Cu_2O_{8+y}$ where R is a rare-earth element, Phys. Rev. B **46**, 11813 (1992).